PAPER

Mesoporous Ni/Ce$_{1-x}$Ni$_x$O$_{2-y}$ heterostructure as an efficient catalyst for converting greenhouse gas to H$_2$ and syngas†

Jie Deng,[ab] Wei Chu,*[a] Bo Wang,[b] Wen Yang[a] and X. S. Zhao*[b]

It has been a great challenge to develop an efficient and stable catalyst for dry reforming of methane with carbon dioxide. A new catalyst was synthesized with the catalytically active component in both the lattice and on the surface of the mesoporous support. A remarkable improvement in the catalytic performance of Ni nanocrystals assembled inside pore channels of mesostructured Ni-doped ceria was observed. The initial activity and long-term stability of the sample substantially surpassed that of samples without the inter-mixed oxide and/or a nonporous architecture, even though the latter was more available. Such an effect concerning a collaborative function stemming from a mesostructure and solid solution has been rarely reported previously in catalysis involving CeO$_2$. We believe that this finding might be of a very generic character and be extended to lots of similar fields. It is expected that the results here can spur experimental and theoretical investigation to promote fundamental comprehension of host–guest or metal–oxide interplay in CeO$_2$-based composite materials.

Introduction

A potential solution is greatly needed to sustainably convert two abundant warming gases (CH$_4$ and CO$_2$) to value-added energy sources or fuels, for mitigating the effects of global climate change. To date, some technologies have been reported using carbon capture–storage–sequestration or photo-electrolysis, while forming solid carbonates by mineralization, and hydrocarbons by hydrogenation, *etc.*[1–6] Another appealing strategy promptly gaining great concern is the one-step catalytic conversion of two warming gases into versatile H$_2$ or syngas (which is viewed as a basic building block or feedstock for many industrially important chemicals) by applying a heat-propelled thermo-chemical process, known as CO$_2$ reforming of methane (CRM).[7–9] This process enables H$_2$-based energy technology and fuel manufacture.

As CRM depends upon heat to propel the endothermic gas phase catalytic reaction, it is operatively very straightforward, and can achieve a higher efficiency than strategies that are built upon photo-electrolysis or traditional electrolysis. In the presence of a supported catalyst, such as metal nanoparticles (NPs) on an oxide, the CRM process proceeds *via* a complex mechanism involving multiple reactions, with the metal

phases responsible for C–H bond cleavage, and the oxide carriers contributing to C–O bond rupture.[7,9]

The stable C–H bonds in CH$_4$ (439 kJ mol^{-1}), and C–O bonds in CO$_2$ (396 kJ mol^{-1}), along with the highly endothermic nature of the CRM process require harsh operating conditions for practical reactant conversion. It is desirable to develop an efficient catalyst which is catalytically reactive at low temperatures and stable at elevated temperatures.[7,8] Nickel (Ni) appears to be one of the most promising catalysts for CRM, though the reaction mechanism is still under debate.[7–9] Unfortunately, Ni NPs can deteriorate rapidly due to sintering of NPs and/or coking. Thus, it is extremely important to develop a stable Ni-based catalyst. The tuned positioning of the building blocks on a nanoscopic level is able to strikingly enhance the behavior of catalysts *via* the electronic and steric interplays.[10] Materials employed for a broad spectrum of industrial, energy-related, environmental, and medical usages have made full use of the synergy between a catalyst and its carrier. Some reducible active metal oxides, *e.g.*, ceria, are able to get involved in catalytic processes *via* either supplying the reactive electron/oxygen by means of producing the vacancy-related defects or altering its oxidation state along with the surface reconstructing with the metal atoms under reaction conditions.[10–13] Under such circumstances, the catalytically active centers are necessarily situated in the intimate vicinity of the interphase boundaries between metallic NPs and oxide substrates.[14,15] It has been well recognized that the dual-center mechanisms wherein reagents can be catalytically activated around the metal/

[a] Department of Chemical Engineering, Sichuan University, Chengdu 610065, China. E-mail: chuwei1965@scu.edu.cn
[b] Department of Chemical Engineering, University of Queensland, Brisbane 4067, Australia. E-mail: george.zhao@uq.edu.au
† Electronic supplementary information (ESI) available. See DOI: 10.1039/c5cy00893j

carrier boundaries are, really, widely present in lots of catalytic cycles.[16]

Assembling metal NPs into mesostructured materials is a peculiar example wherein the metal/carrier interplays can be notably reinforced by nanoconfinement effects.[17] The tight surrounding of metal NPs by the concave internal surfaces of physically nanosized channels can optimize the metal/carrier interfaces, resulting in state-of-the-art composites for various usages. In addition to the likelihood of the enhanced activity, this metal NP in-pore assembly provides an effective means for, to a maximum extent, restricting the deterioration of catalysts due to clustering of metal NPs.[18–22] Besides, stabilizing active metal phases by well-structured oxide precursors such as perovskites and solid solutions gives a robust way to tune the catalytic properties of metal NPs.[23,24] Among them, the mixed metal oxide system is compelling as a promising nanocomposite in catalytic applications due to some distinct chemical properties from single metal oxides.[25–27] Inserting the second metal into the host lattice of the oxide carrier might reinforce the carrier–metal interplay and consequently influence the electronic characteristics of the metal and carrier to generate superficial centers, which are highly reactive for breaking the C–H and C–O bonds present in reagents. On crystalline microstructural levels, the second metal can exert strain on the bulk matrix of the oxide, leading to, in such a manner, generation of defective sites which might impact the immobilization of the loaded active component over oxide surfaces and change the redox functions of the whole system resulting in a better oxygen accessibility. Such effects are especially remarkable for reactions under severe conditions, as is the case for CRM.

In this work, a new mesostructured Ni/Ni-doped CeO_2 hetero-nanocatalyst (labelled as Ni/mp-$Ce_{1-x}Ni_xO_{2-y}$) was synthesized and studied, with kinetic robustness against coking and Ni-sintering, thus presenting good CRM behavior. The Ni–CeO_2 material is a kind of composite widely applied for various reactions such as CO oxidation/methanation, CH_4 decomposition, the water-gas shift reaction, the hydrogenation reaction, biomass reforming, and in solid oxide fuel cells,[28–32] but is largely unexploited for CRM. We believe that the H_2 energy and syngas production from two greenhouse gases in the Ni-supported mesoporous Ce–Ni solid solution shown here is an example rarely reported previously, wherein the reactivity and stability of the Ni-catalyzed gas-phase CRM process benefits substantially from occurring within a Ni-confined $Ce_{1-x}Ni_xO_{2-y}$ mesostructure. We prepared Ni/mp-$Ce_{1-x}Ni_xO_{2-y}$ heterostructures using a new and facile microwave-aided reflux coprecipitation protocol. Our strategy was to achieve a redox-active and thermo-stable heterostructure from a cubic fluorite-type ceria by simply doping Ni^{2+} on the Ce^{4+} sites and introducing mesoporous frameworks.

Experimental

Catalyst preparation

For comparison, the pristine Ni/CeO_2 sample with the same Ni loading was derived by common wet incipient impregnation using pure CeO_2 as the support. The new $Ni/Ce_{1-x}Ni_xO_{2-y}$ samples were derived by a coprecipitation strategy employing $Ni(NO_3)_2 \cdot 6H_2O$ and $Ce(NO_3)_3 \cdot 6H_2O$ as precursors and NaOH (aq 0.2 M) as a precipitate agent. First, each nitrate was dissolved into pure deionized H_2O separately, and then the solutions were mixed to derive a 0.1 M nitrate solution with molar ratios of Ce to Ni of 3 : 1 (labelled as solution A); meanwhile NaOH was dissolved into pure deionized H_2O to form a 0.2 M solution (labelled as solution B). Then, coprecipitation was conducted by mixing solutions of A and B under strong magnetic stirring, and the pH during coprecipitation was stabilized at 11. For the purpose of deriving the anticipated mesostructure, P123 was employed as the template during the coprecipitation. After finishing coprecipitation, the resulting suspension was placed in an advanced microwave system to experience 1 h aging treatment, and the microwave oven power was set to 450 W. The final slurry was subjected to washing and drying overnight at 80 °C. To stabilize the mesoporous framework, the as-prepared powders were thermally annealed at the low temperature of 200 °C for 4 h. Afterwards, the products were refluxed with ethylene diamine (EN) aqueous solution for 48 h in the temperature range of 90–100 °C, and during reflux the pH value was fixed at roughly 11.[33] Subsequently, the derived powders were filtered several times by pure deionized water, and dried overnight at 80 °C. Finally, the resultant products were initially thermally treated at 350 °C under N_2 for 4 h to stabilize the mesoporous framework and afterwards at 600 °C in air for 2 h to eliminate the organic template and enhance the crystallinity. Another $Ni/Ce_{1-x}Ni_xO_{2-y}$ catalyst with no utilization of the P123 template in the precursor solution was likewise synthesized. The catalytic material with and without utilization of P123 was referred to as Ni/mp-$Ce_{1-x}Ni_xO_{2-y}$ and Ni/n-$Ce_{1-x}Ni_xO_{2-y}$.

Characterization

Chemisorption of H_2 was conducted in an auto chemisorption analyzer. The samples were first dried in helium at 250 °C for 2 h and reduced *in situ* by H_2 at 450 °C for 1 h at a ramp of 10 °C min^{-1}. The catalysts were flushed by helium at the reduction temperature for 2 h, and afterwards cooled down to 30 °C in vacuum to implement the chemisorption tests. H_2-temperature programmed reduction (H_2-TPR) was carried out with a fixed-bed reactor. The sample was subjected to 4.2% H_2/N_2 mixed gas (30 mL min^{-1}) from 100 to 800 °C at a heating rate of 5 °C min^{-1}. The H_2 evolution was detected online by a SC-200 gas chromatograph with a thermal conductivity detector (TCD). X-ray diffraction (XRD) patterns were obtained with a Rigaku diffractometer using Cu K$_\alpha$ radiation. N_2 adsorption–desorption isotherms at −196 °C were measured on tristar II 3020. Initially, all samples were degassed at 200 °C for 16 h before the tests. The specific surface areas were computed employing the Brunauer–Emmett–Teller (BET) equations. Raman spectra of the catalysts were recorded using an excitation wavelength of 514 nm

(visible) or 325 nm (UV) on a Renishaw (RM2000) spectrometer. The element contents were obtained *via* inductively coupled plasma atomic emission spectrometry (ICP-AES). Thermogravimetric analysis (TGA) was performed on a Q500 thermogravimetric analyzer. The catalysts were heated in flowing air from 25 °C to 800 °C at a ramp of 10 °C min^{-1}. Scanning electron microscopy (SEM) analysis of the samples was made using JEOL 7001, 6300 field-emission scanning electron microscopy (FESEM). The UV-vis DRS measurements were performed over the wavelength range 200–800 nm using a PERSEE TU-1901 UV-vis NIR spectrophotometer with an integration sphere diffuse reflectance attachment. Samples were diluted in a KBr matrix by pelletization.

Reactivity assessment

The catalytic performances were measured under atmospheric pressure utilizing a continuous fixed-bed flow reactor. Typically, the catalyst sample was diluted with inert SiO_2 and charged into the reactor using quartz wool. A reactant feed made up of a gaseous mixture of CH_4/CO_2 with a GHSV of 12 000 mL (h g$_{cat}$)$^{-1}$ was adopted. The catalyst was pre-treated with H_2 at 450 °C for 1 h before the tests. The outlet gases from the reactor were analyzed online by a GC-1690 model gas chromatograph (fitted with a TDX01 column) equipped with a thermal conductivity detector (TCD).

Results and discussion

Structural and textural properties of the as-prepared samples

The textural properties were examined by N_2 volumetry. As shown in Fig. 1, a typical type-IV isotherm with a H1 hysteresis loop, characterized by a well-defined and steep step of N_2 uptake in a wide relative pressure (P/P^o) range of 0.55–0.90, is seen on Ni/mp-Ce$_{1-x}$Ni$_x$O$_{2-y}$, verifying the mesoporosity of a mesoporous channel, while this hysteretic behavior was absent for Ni/n-Ce$_{1-x}$Ni$_x$O$_{2-y}$ and Ni/CeO$_2$, revealing the nonporous nature. The initial part of the isotherm was as a result of monolayer–multilayer adsorption, and the hysteretic loop was related to capillary condensations occurring inside the mesopores.[33–35] The isotherm data indicated that employing P123 as the template was robust for constructing a mesostructured skeleton in reflux phases. Because the as-prepared samples were thermally annealed at as high a temperature as 600 °C, the results clearly indicted that the

formed mesostructure can withstand the demanding thermo-conditions. This is an important property for the CRM application. The good thermo-durability of this skeleton was ensured by both the inherently structural and chemical stability of the CeO$_2$ carrier and by the encircling EN protector that can effectively stabilize the mesoporous network against collapse during thermal annealing.[33] The Barrett–Joyner–Halenda (BJH) pore diameter for Ni/mp-Ce$_{1-x}$Ni$_x$O$_{2-y}$ was on average 8.5 nm. In sharp contrast with the other two samples, the Brunauer–Emmett–Teller (BET) specific surface area and the total pore volume for Ni/mp-Ce$_{1-x}$Ni$_x$O$_{2-y}$ were considerably larger (specific surface area: 20.8, 89.4, and 205.1 m^2 g^{-1} for Ni/CeO$_2$, Ni/n-Ce$_{1-x}$Ni$_x$O$_{2-y}$, and Ni/mp-Ce$_{1-x}$Ni$_x$O$_{2-y}$, respectively; total pore volume: 0.031, 0.086, and 0.426 m^3 g^{-1} for Ni/CeO$_2$, Ni/n-Ce$_{1-x}$Ni$_x$O$_{2-y}$, and Ni/mp-Ce$_{1-x}$Ni$_x$O$_{2-y}$, respectively), also unravelling the well-developed mesopore system.

The phase structure was analysed by X-ray diffraction (Fig. 2a). All samples showed major contributions at 28.5°, 33.1°, 47.5°, 56.3°, 59.1°, 69.4°, 76.7°, and 79.1°, which can be indexed to (111), (200), (220), (311), (222), (400), (331), and (420) of the face-centred cubic (fcc) fluorite-type structure of ceria, respectively.[36] The broadening of these diffraction peaks for the mesostructure hinted at the nanocrystalline nature of the channels of mesoporous materials, meanwhile revealing that the mesostructure can effectively downsize the ceria grain. According to prior studies, this effect of stabilizing the ceria grain size can be due to the EN species that effectively protected the mesostructured ceria primary grains, and hence prolonged the improvement in the crystallization for ceria and retarded the ceria grain aggregation.[33] The peaks linked with the NiO phases were absent for both the coprecipitated samples yet were found for Ni/CeO$_2$, unveiling that the Ni species were highly dispersed (<4 nm) or incorporated into ceria lattices to form the solid solution for Ni/mp-Ce$_{1-x}$Ni$_x$O$_{2-y}$ and Ni/n-Ce$_{1-x}$Ni$_x$O$_{2-y}$ but were present on the ceria surfaces in the form of large-sized NiO crystallites for Ni/CeO$_2$.[37,38] By closely comparing the (111) diffraction lines for the fluorite structure (Fig. 2b), it can be clearly seen that, in comparison with the pure ceria, the position shifted leftward for Ni/mp-Ce$_{1-x}$Ni$_x$O$_{2-y}$ and Ni/n-Ce$_{1-x}$Ni$_x$O$_{2-y}$ but remained nearly unchanged for Ni/CeO$_2$, evidencing that the Ni^{2+} ions were successfully incorporated into the ceria lattice
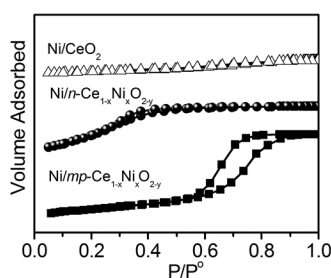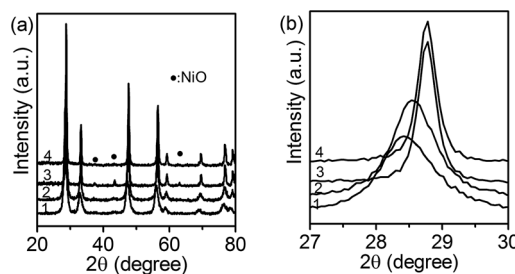

Fig. 1 Isotherms of all samples.

Fig. 2 (a) XRD patterns of fresh Ni/mp-Ce$_{1-x}$Ni$_x$O$_{2-y}$ (1), Ni/n-Ce$_{1-x}$Ni$_x$O$_{2-y}$ (2), Ni/CeO$_2$ (3), and CeO$_2$ (4). (b) The corresponding enlargement of the (111) diffraction lines shown in (a).

to form a solid solution with the typical cubic fluorite structure for the binary mixed system, whereas, they were practically all present as crystalline NiO phases on the ceria surfaces for the impregnated sample.[39] Quantitative analysis using the ICP tool (samples were treated with HNO_3 before testing to remove the surface Ni species as described in the previously published literature[40]) showed that the accurate content of Ni confined inside the bulk ceria was 13.8%, 0.3%, and 10.6%, for Ni/mp-Ce$_{1-x}$Ni$_x$O$_{2-y}$, Ni/CeO$_2$, and Ni/n-Ce$_{1-x}$Ni$_x$O$_{2-y}$, respectively. As shown in Table S1,† the Ni NP size is only 3.9–5.2 nm on two mixed samples and as big as 10–13 nm on Ni/CeO$_2$. The Ni dispersion is 7.9% on Ni/CeO$_2$, 19.2% on Ni/n-Ce$_{1-x}$Ni$_x$O$_{2-y}$, and 25.1% on Ni/mp-Ce$_{1-x}$Ni$_x$O$_{2-y}$, while the Ni surface area is 1.82 m^2 g^{-1} on Ni/CeO$_2$, 2.53 m^2 g^{-1} on Ni/n-Ce$_{1-x}$Ni$_x$O$_{2-y}$, and 2.91 m^2 g^{-1} on Ni/mp-Ce$_{1-x}$Ni$_x$O$_{2-y}$. This shows that the surface Ni species on the two mixed samples were very dispersed and exposed. Altogether, for mixed oxides, most of the Ni atoms were embedded in the ceria lattice to produce the solid solution, while the rest were highly dispersed on the solid solution surfaces to form a periodic structure of NiO.

In fact, as illustrated in Scheme 1, the steadiest Ce or Ni oxide adopts distinct crystalline configurations and a formal valance status (4+ and 2+, respectively); the coordinative number is 8 for the Ce cations whereas it is 6 for the Ni cations.[41,42] It can be predicted that, when replacing Ce cations in a ceria lattice with Ni cations, the appreciable electronic and structural perturbations (such as stress, point and defects, and oxygen vacancies) in the host lattice and the extrinsic defects both near the grain boundaries and on the plane surfaces would occur, causing the shrinkage or expansion of the lattice parameter of the unit cell. In principle, when the oxidation state of alien ions is steadily 4+, we can predict the lattice parameter fluctuation by directly comparing the relative radius of two ions;[43–46] however, with the charge of the alien ions unequal to that of Ce^{4+}, the lattice volume change will be governed by some other factors and not only by the ion radius disparity.[47–49] In the case of the intermixed oxide of Ni in CeO$_2$, this situation is very complex. Some authors observed lattice contraction after Ni^{2+} substitution for Ce^{4+}.[29] In contrast, in our case, a cell expansion, as reflected by the leftward shift of the ceria-assigned diffraction lines, was found. This expansion essentially arose from a combined effect by the ion radius disparity between Ni^{2+} (72 Å) and Ce^{4+} (92 Å) and the formation of the oxygen vacancy-related defects inside the ceria lattice. After the
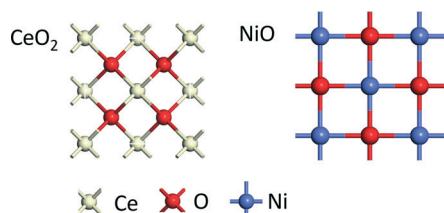
isomorphic substitution of Ni^{2+} for Ce^{4+}, the charge difference between cations induced the charge imbalance in the ceria lattice. To maintain electroneutrality, the formation of oxygen vacancies and Ce^{3+} centers along with alterations in local structures emerged. The much greater ion radius of Ce^{3+} than Ce^{4+} is able to overcome, offset, or compensate the diameter disparity between Ni^{2+} and Ce^{4+}, thereby inducing the lattice expansion. To verify this inference, next, we closely analysed the structural and electronic perturbations of all samples.

Bulk and surface defects

Raman spectroscopy was used for elucidating the bulk and surface structural defects because it is sensitive to vibrational structures of both the M–O arrangement and lattice defects. The visible excitation laser line can penetrate into the deep inner layers of CeO$_2$ and thus reflect the bulk information of CeO$_2$. As shown in Fig. 3a, for all samples, the predominant strong peaks centred at 460 cm^{-1} are characteristic of the first-order Raman active mode of the fluorite-type lattice (F_{2g}), which can be viewed as an intrinsic symmetric breathing mode of oxygen atoms around cerium ions (O–Ce–O).[50–55] Compared to ceria and the impregnated sample, broadening and red shift of this mode on coprecipitated samples, particularly for Ni/mp-Ce$_{1-x}$Ni$_x$O$_{2-y}$, were observed. This change in F_{2g} was attributed to the variation in the M–O vibration frequency when substituted with the dopant, which accounts for the disparity in the ionic radius. The ionic radius disparity between cations allows the lattice parameter variations because of cell shrinkage or expansion. Hence, vibrations are rapid for a shrunken lattice and slow down for an expanded lattice so that the band
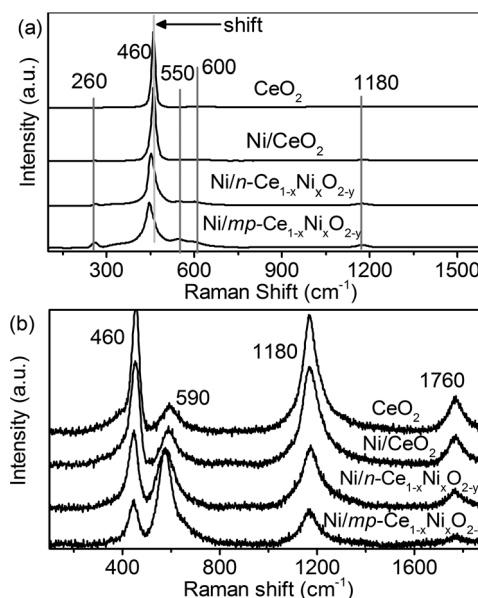

Fig. 3 Visible (λ_{ex} = 514 nm) (a) and UV (λ_{ex} = 325 nm) (b) Raman spectra of all samples.

Scheme 1 Crystal structure of CeO$_2$ and NiO.

shifted to higher and lower wave numbers, respectively.[50–54] These reflected that the symmetry of the cubic fluorite structure was notably disturbed and lowered due to the changed lattice spacing and Ce–O bond distance. Besides, on coprecipitated samples, some well-defined weak second-order Raman bands, which pertained to the lattice disorder or defects in the ceria lattice such as oxygen vacancies, phonon confinement, or inhomogeneous strain, were detected near 260 cm^{-1}, 550 cm^{-1}, 600 cm^{-1}, and 1180 cm^{-1}, further confirming the formation of $Ce_{1-x}Ni_xO_{2-y}$ solid solution with the Ni^{2+} ions replacing the Ce^{4+} ions in the CeO_2 lattice. The bands around 600 cm^{-1} represented the longitudinal optical (LO) mode of ceria, which stems from the relaxation of symmetry rules that can be associated with the intrinsic defects in the ceria lattice. This was attributed to a localized substitution defect vibration. These intrinsic defects were reportedly either Ce^{3+} trapped in octahedral sites, or vacancy-interstitial (Frenkel-type) oxygen defects, which were formed in the way that oxygen anions in ceria relocate themselves from tetrahedral sites to octahedral sites leaving vacancies in tetrahedral sites and localizing the excess electrons on the adjacent Ce cations.[51] The bands emerging at 550 cm^{-1} belonged to the defect-induced modes (D band), which were possibly responsible for the Ce–O–Ni bonds or oxygen vacancies induced inside the ceria lattices to keep electroneutrality upon replacement of Ce^{4+} with Ni^{2+}. The peaks at 260 cm^{-1} corresponded to the second-order transverse acoustic (2TA) mode of ceria while the one at 1180 cm^{-1} corresponded to the second-order longitudinal (2LO) mode of ceria.[50–55]

Due to the resonance Raman effect, the samples can strongly adsorb in the UV region, and thus the UV laser line detected the outer surface information of ceria. As shown in Fig. 3b, when employing the UV laser line (325 nm), the bands at 550 and 600 cm^{-1} conflated as a wide peak and the peaks near 460 cm^{-1} got substantially attenuated relative to those with an applied visible laser line. The 2LO band was as intense as the F_{2g} mode while the third overtone band (3LO) likewise arose near 1760 cm^{-1}. This marked intensification for the LO overtones under UV excitation originated from the multiphonon excitation by the resonance Raman effect. In addition, the LO mode possessed a similar strength to the F_{2g} mode. As for Ni/mp-$Ce_{1-x}Ni_xO_{2-y}$, the LO band exceeded the F_{2g} mode in intensity, which clearly indicated that there were the most surface defect sites on Ni/mp-$Ce_{1-x}Ni_xO_{2-y}$, in line with the previous report that the inner concave surfaces of mesoporous walls can expose more defects or exert strain. So, the mesostructure showed a preference for increasing the surface defects. This may be as a result of the crystallographic surface termination by the different morphostructure or the area–volume effect by the large specific surface area and small grain size. The relative intensity ratio of $(I_D + I_{LO})/I_{F_{2g}}$ mirrored the defect concentration such as oxygen vacancies, and it followed the sequence: Ni/mp-$Ce_{1-x}Ni_xO_{2-y}$ > Ni/n-$Ce_{1-x}Ni_xO_{2-y}$ > Ni/CeO_2. Conversely, the NiO-indexed bands near 520 cm^{-1} were not discernable, very possibly because of a shadowing effect by the long tailing of the F_{2g} mode.

Surface oxidation state

UV-vis DRS was employed to gain insights into the surface coordination and different oxidation states of samples by checking the d–d and f–d transitions and the oxygen–metal ion charge transfer bands. As shown in Fig. 4, the pure CeO_2 presented three absorption maxima near 255 nm, 285 nm, and 340 nm. The latter two well-resolved absorption maxima corresponded to the $O^{2-} \rightarrow Ce^{4+}$ charge transfer and interband transitions, respectively, and the poorly identified former one was ascribed to the $O^{2-} \rightarrow Ce^{3+}$ charge transfer transition.[56–58] For both intermixed oxides, in particular Ni/mp-$Ce_{1-x}Ni_xO_{2-y}$, absorption enhancement and a band shift obviously occurred, suggesting an increase in the low-coordinated cerium cations. The red shift of the inter-band transition can arise from the existence of Ni^{2+}, which induced a pronounced rise in the Ce^{3+} concentration over surfaces, thus increasing the charge transfer gap between the O2p and Ce4f orbitals. The blue shift of the charge transfer transitions implicated the occurrence of abundant oxygen vacancies. Hence, the UV-vis DRS confirmed that doping with Ni^{2+} at the Ce^{4+} sites of the mesostructured CeO_2 indeed facilitated the formation of the undercoordinated Ce^{3+}, increased the oxygen vacancy concentration, and induced the charge redistribution-compensation mechanism.

Redox properties

Taken together, it can be clearly seen from above that a Ni NP-confined mesoporous Ce–Ni solid solution with noted structural and electronic perturbations was derived. A crucial first evaluation on the feasibility of this material in CRM usage is to identify the degree of redox kinetics and the ability for oxygen mobility. Shown in Fig. 5 is the temperature-programmed reduction by H_2 of all samples. There emerged two envelopes for the pure CeO_2: a very weak one at 655 °C (γ_1) and a big broad one ranging from 780 °C to 900 °C (γ_2), which were relevant to the reduction of the outermost and innermost shell lattice oxygen of ceria, respectively.[59] The nanosized NiO gave a single symmetric peak at 320 °C (β). For Ni/CeO_2, the peak centred at 380 °C (β_2) belonged to large aggregated NiO particles. The shift of the reduction temperature to a high temperature was caused by the large granule size (as verified by XRD data) which retarded the H_2
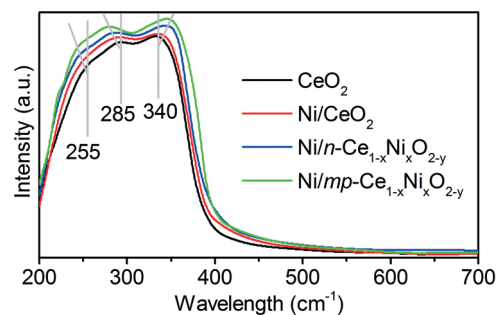

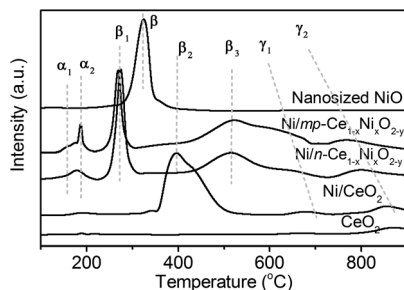Fig. 4 UV-vis diffuse reflectance spectra of all samples.

Fig. 5 TPR profiles of pure CeO_2, Ni/CeO_2, Ni/n-$Ce_{1-x}Ni_xO_{2-y}$, Ni/mp-$Ce_{1-x}Ni_xO_{2-y}$, and nanosized NiO.

diffusion inside the particulate to complete its reduction.[37,60] However, the hydrogen consumption for the mixed phase oxides was distinct from that for Ni/CeO_2, and divided into the multiple well-characterized regions. The low temperature peaks below 230 °C (α_1 and α_2) were assigned to the surface oxygen species adsorbed on the surface oxygen vacancies, caused by the generation of Ce–Ni solid solutions.[61] As discussed above, the solid solution was formed by dissolution of Ni^{2+} in the CeO_2 lattice to replace Ce^{4+}, and thus the charge imbalance and lattice distortion in CeO_2 resulted in oxygen vacancies that adsorbed oxygen molecules on oxide surfaces. These adsorbed oxygen molecules were very reactive oxygen species and were ready to be reduced by H_2 at low temperatures. Therefore, the intensity of the α_1 and α_2 region can be determined by the population of oxygen vacancies on oxide surfaces; consistent with the structural and electronic analysis, the particular architecture of Ni/mp-$Ce_{1-x}Ni_xO_{2-y}$ can adsorb the affluent oxygen species over the surfaces. This is also a critical indicator for excellent oxygen mobility to enhance the carbon removal rate during CRM.

The reductive process of Ni for mixed metal oxides evolved into two different steps. The peaks near 270 °C (β_1) with a low temperature tail were responsible for the highly dispersed NiO species on the intermixed metal oxide matrix surfaces because the very small Ni particles can expose more surfaces to H_2.[62] The peaks centred at 515 °C (β_3) were due to the complex NiO species which strongly interacted with CeO_2.[63] Integrated with the structural data, it can be indexed to the Ni species included inside the CeO_2 lattice. The considerably higher reduction temperature than the pure, aggregated, or highly dispersed NiO species clearly showed that the Ni–O bond in the solid solutions was stronger than that in the bulk NiO. This strong Ni–O bond in the solid solution arises from the fact that when occupying the Ce^{4+} sites the Ni^{2+} was forced to possess a very large number of oxygen neighbours forming the stronger $Ni \leftrightarrow O \leftrightarrow Ce$ exchange in the fluorite structure than the $Ni \leftrightarrow O \leftrightarrow Ni$ interaction in the rock salt structure. The wide bumps at 550 °C, as the shoulder peaks of β_3, represented γ_1, hinting that the reduction of Ni inside CeO_2 was simultaneously accompanied by the reduction of surface lattice O^{2-} anions. The reduction of the bulk ceria (γ_2) shifted to as low a temperature as 720 °C, nearly 100 °C lower than that of the pure

CeO_2. The maximum reduction temperatures of γ_1 and γ_2 on Ni/mp-$Ce_{1-x}Ni_xO_{2-y}$ were about 40 °C and 50 °C lower than those of Ni/n-$Ce_{1-x}Ni_xO_{2-y}$, respectively, and their peak intensity was larger. Notably, γ_1 got merged with β_3 to a big wide peak on Ni/mp-$Ce_{1-x}Ni_xO_{2-y}$ but got separated from β_3 on Ni/n-$Ce_{1-x}Ni_xO_{2-y}$, hinting at the smaller activation barrier for removing O species in fluorite structures on Ni/mp-$Ce_{1-x}Ni_xO_{2-y}$. Given the structural data, its good redox ability may stem from big surface areas and more stress/defects in the bulk. The large surface exposes more surface Ce ions. Due to the distinct micro-chemical environment between the CeO_2 surface and the bulk, surface Ce ions are prone to having a low coordination number. Thus, more surface undercoordinated Ce ions were seen on Ni/mp-$Ce_{1-x}Ni_xO_{2-y}$. As surface O atoms are bonded by fewer nearest neighbours (lower coordination number than the bulk), they will be readily mobile/removable. The stress and defects in the solid solution caused the CeO_2 lattice to expand, destabilizing the fluorite structure and weakening the Ce–O bond. Thus, O^{2-} anions around the Ce cations became more easily removed by H_2. In addition, the highly dispersed Ni particles were easily reducible at low temperatures, which can cause the H species activated on the NiO surfaces to spill over onto the fluorite structure, further catalysing the reduction of CeO_2.

Indeed, the H_2-TPR data implied a robust synergy between the Ni and Ce species which substantially favoured the redox kinetics of Ni/mp-$Ce_{1-x}Ni_xO_{2-y}$. This reduction depth directly amounted to the larger cycle capability and thus possibly more efficient generation of H_2 energy and syngas supposing that the re-oxidation of CeO_2 with CO_2 was adequately facilitated. The much lower onset temperature for removing the oxygen species of the fluorite structure unequivocally meant that the Ni/mp-$Ce_{1-x}Ni_xO_{2-y}$ heterostructure potentially had a smaller reduction enthalpy (or a lower oxygen diffusion/activation energy barrier) than the other samples. Lately, the reduction enthalpy has been considered as a critical indicator to appraise the feasibility of the candidate catalysts for application to CRM.[7–9] On the whole, the magnitude of the reduction enthalpy or the oxygen diffusion/activation energy barrier determined the rate boundaries at which the support-mediated redox catalytic cycle could be well established. The typical redox behavior for Ni/CeO_2 put this material under the circumstance of the oxygen accessibility being much lower. In sharp contrast, it can be envisaged that the Ni/mp-$Ce_{1-x}Ni_xO_{2-y}$ composite trended in a better direction since the H_2 energy and syngas generation under typical CRM conditions (600–800 °C) will proceed well with the Ni metal phase being active for C–H bond cleavage to form CH_x species and H_2, and the oxide carrier providing sufficient oxygen species by activating CO_2 to oxidize CH_x into syngas.

Catalytic performance improved by heterostructure

The initial catalytic activity as a function of temperature is shown in Fig. 6. The initial catalytic reactivity was found to
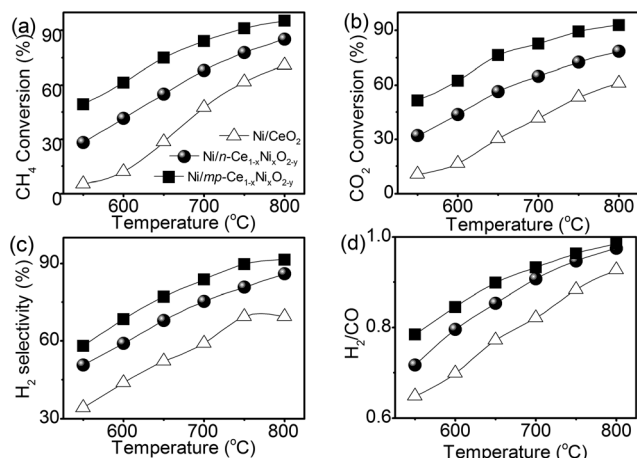
Fig. 6 The effect of temperature on CH_4 conversion (a), CO_2 conversion (b), H_2 selectivity (c), and H_2/CO ratio (d) over all samples.

be strongly dependent upon the reaction temperature. Both CO_2 and CH_4 conversions for all samples significantly increased with the increment in the reaction temperatures, revealing the endothermic nature of CRM. All catalysts presented their greatest initial reactivity at 800 °C in the temperature range investigated. In addition, the CO_2 conversion was larger than that of CH_4 for all catalysts at a low temperature below 700 °C. This was caused by the concurrent occurrence of the reverse water-gas shift (RWGS) reaction (CO_2 + $H_2 \rightleftharpoons H_2O + CO$). Nonetheless, a greater CH_4 conversion than that of CO_2 was seen for all samples between 750 and 800 °C. This can be contributed to by two factors: the exothermic RWGS was oppressed when ramping up the reaction temperatures, and the thermodynamically favourable CH_4 decomposition occurred violently at high reaction temperatures. Analogous behaviors for Ni-based catalysts have also been reported before.[64] Most noticeably, much higher reactant conversions were discovered on Ni/mp-Ce$_{1-x}$Ni$_x$O$_{2-y}$ relative to Ni/n-Ce$_{1-x}$Ni$_x$O$_{2-y}$ at the same temperatures in the whole temperature range studied, while Ni/n-Ce$_{1-x}$Ni$_x$O$_{2-y}$ exhibited a higher activity than the conventionally impregnated Ni/CeO$_2$. Such disparity can be the cooperative result of the high dispersion, good redox ability, and large specific surface area. The highly dispersed Ni nanoparticles were well confined or distributed in the pore channels of the redox-active and large specific surface area solid solution; therefore, more active sites were provided and the catalyst can contact and interact with reactants adequately.

The H_2 selectivity (Fig. 6c) shows a similar trend to the reactant conversion, and this was owing to the fact that the elevated reaction temperature facilitated H_2 production *via* different reactions, for example, the water-gas shift reaction (WGS), carbon gasification, and CH_4 decomposition. These reactions more preferentially took place at elevated temperatures and could have generated H_2. Ni/mp-Ce$_{1-x}$Ni$_x$O$_{2-y}$ yielded a notably larger H_2 selectivity than any other two samples. The H_2 selectivity at 700 °C was 83.8%, 75.4%,

and 59.1% for Ni/mp-Ce$_{1-x}$Ni$_x$O$_{2-y}$, Ni/n-Ce$_{1-x}$Ni$_x$O$_{2-y}$, and Ni/CeO$_2$, respectively.

The H_2/CO ratio (Fig. 6d) was between 0.6 and 1.1 over the whole temperature range investigated and rose with the increasing temperature. This value was substantially below unity particularly at the low temperatures because H_2 was consumed at a low temperature by side reactions such as the RWGS, or the methanation reaction. Yet, it increasingly approached unity at the elevated temperature, due to the fact that the high temperature favoured the formation of H_2 by means of the WGS, carbon oxidization, and CH_4 cracking. Among all the samples, this ratio approached the CRM stoichiometric value the most at each temperature while employing the Ni/mp-Ce$_{1-x}$Ni$_x$O$_{2-y}$ material, manifesting that the fewest side reactions occurred over this material in the course of the reaction. The discrepancy among the three catalysts in terms of the initial reactivity and H_2/CO ratio signified an appreciably positive impact imparted by this particular catalyst configuration of Ni/mp-Ce$_{1-x}$Ni$_x$O$_{2-y}$. This promoting effect was even more encouraging considering that the diffusion of reactants and products into and out of the pore channels ought to impede the reaction to some degree in comparison with that on the freely accessible open surfaces. Apparently, the remarkably various reactivity of Ni/mp-Ce$_{1-x}$Ni$_x$O$_{2-y}$, Ni/n-Ce$_{1-x}$Ni$_x$O$_{2-y}$, and Ni/CeO$_2$ cannot be linked with the number of particles since the loadings of the active Ni phase in the three samples and the original diameter of the Ni particulates in both coprecipitated samples were analogous. In addition, the exclusive contribution from the geometrical impacts of the pore channels upon the catalytic functions within the mesoporous Ce–Ni solid solution were excluded using a comparison test with the mesoporous silica SBA-15 functioning as the catalyst carrier, which gave an obviously poorer reactivity than Ni/mp-Ce$_{1-x}$Ni$_x$O$_{2-y}$ (Fig. 7), despite the fact that SBA-15 also had an analogous cylindrical channel with a pore diameter of 7–8 nm, and hence can impart an analogous dimensional or steric confinement for the Ni metal grains. This showed that the pore walls actually participated in the mechanic process by boosting the metal/carrier synergy. Detailed reasons for selecting Ni/SBA-15 as the control test can be found in the ESI.†

A final appraisal of the catalyst practicability for CRM is stability. To compromise the catalytic performance and energy consumption, 700 °C was opted for as the optimal
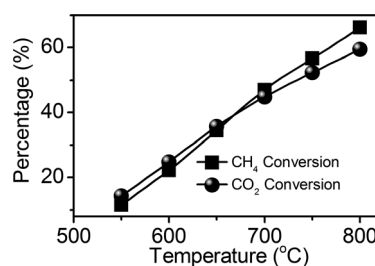

Fig. 7 Initial activity on the Ni-SBA-15 catalyst.

reaction temperature to assess the long-term durability of materials within this study, and the results are shown in Fig. 8. For Ni/mp-Ce$_{1-x}$Ni$_x$O$_{2-y}$, the invariable level of the converted reactants plus the formed H$_2$ and CO during the 2400 min test was inspiring and suggested that the performance remained stable and there was no material degeneration mechanism in action. The CH$_4$ conversion, which was nearly identical to the CO$_2$ conversion when they changed with the time on stream, coincided with the stoichiometric coefficients for CRM. This excellent behavior must be only relevant to the particular Ni NP-confined fluorite type Ce–Ni solid solution mesostructure. In accordance with the trend for the initial activity data in Fig. 6, Ni/n-Ce$_{1-x}$Ni$_x$O$_{2-y}$ gave an activity and stability that was relatively inferior to Ni/mp-Ce$_{1-x}$Ni$_x$O$_{2-y}$ but much superior to Ni/CeO$_2$. The CH$_4$ and CO$_2$ conversion somewhat declined from 67.9% and 64.7% to 40.3% and 52.6%, respectively, indicating that a moderate decay occurred for Ni/n-Ce$_{1-x}$Ni$_x$O$_{2-y}$. Nevertheless, for Ni/CeO$_2$, both the CH$_4$ and CO$_2$ conversion sharply plummeted from 47.8% and 41.6% to 23.6% and 23.2% even only after 1200 min of time on stream, while the CO and H$_2$ selectivity as well as the H$_2$/CO ratio decreased significantly. For both Ni/n-Ce$_{1-x}$Ni$_x$O$_{2-y}$ and Ni/CeO$_2$, the CH$_4$ conversion was lower than the CO$_2$ conversion, implying a serious imbalance for the formation rate between the CH$_x$ and the CO$_2$-derived O species during the stability test. Combined with the observations that the H$_2$/CO ratio was smaller than the ideal value (unity) and a small quantity of water was detected in the cold trap, it can be inferred that this high CO$_2$ consumption was caused by the occurrence of the reverse water-gas shift instead of its direct dissociation activation by the defect sites on CeO$_2$. The production of H$_2$O has been shown to be able to accelerate sintering of nickel metal particles. The poor activity and unexpected product distribution for Ni/n-Ce$_{1-x}$Ni$_x$O$_{2-y}$ and Ni/CeO$_2$ revealed a lack of available reactive sites for CRM. Overall, the catalytic stability for all materials increased in the

following sequence: Ni/CeO$_2$ < Ni/n-Ce$_{1-x}$Ni$_x$O$_{2-y}$ < Ni/mp-Ce$_{1-x}$Ni$_x$O$_{2-y}$.

Characteristics of spent catalysts

According to previous studies,[65,66] the catalytic activity decay during CO$_2$–CH$_4$ reforming was mainly due to coking occurring over active sites. The main pathway for generating the carbon residuals can proceed as follows:

$$2CO \rightarrow C + CO_2 \text{ (Boudouard reaction)}$$

$$CH_4 \rightarrow C + 2H_2 \text{ (cracking)}$$

The carbon deposits formed can be eliminated by oxidation (O + C → CO or 2C + 2OH$^-$ → CO + H$_2$O).

The spent samples were analysed using XRD, SEM, and TG-DTA to study the reasons behind the catalytic degradation. In the XRD data (Fig. 9), the used Ni/mp-Ce$_{1-x}$Ni$_x$O$_{2-y}$ nearly presented the same pattern as the fresh one, save that the CeO$_2$ crystallinities grew slightly. Importantly, the indistinguishability of the Ni phase-assigned diffraction peaks clearly suggested that the highly dispersed small-sized Ni crystals were effectively stabilized during the CRM reaction. However, for other spent samples, in particular Ni/CeO$_2$, strong signals for Ni species near 44° and graphitized carbons at 26° emerged, demonstrating that severe Ni sintering and carbon deposition occurred during the reaction. Quantitatively (Table S1†), the Ni NP size is still below 6 nm on Ni/mp-Ce$_{1-x}$Ni$_x$O$_{2-y}$ but notably grew to 13–17 nm on Ni/n-Ce$_{1-x}$Ni$_x$O$_{2-y}$ and 22–28 nm on Ni/CeO$_2$ after the reaction; the Ni surface area and dispersion were kept on Ni/mp-Ce$_{1-x}$Ni$_x$O$_{2-y}$ but fell sharply over others. In the SEM micrographs (Fig. 10), carbon filaments are observed on used Ni/CeO$_2$ and Ni/n-Ce$_{1-x}$Ni$_x$O$_{2-y}$ but are practically invisible on Ni/mp-Ce$_{1-x}$Ni$_x$O$_{2-y}$. The amount of carbon filaments was greatest for Ni/CeO$_2$. Thus, the graphitic peaks observed in the XRD data can reasonably be ascribed to the carbon filament deposits.

TG-DTA analysis (Fig. 11) was used to quantify the overall amounts of carbon species and identify their types and thermal stability. The total weight loss derived from gasification of carbon species decreased in the following order:
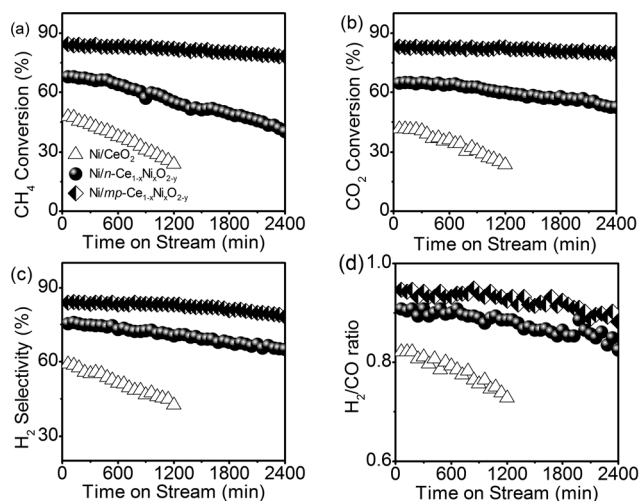

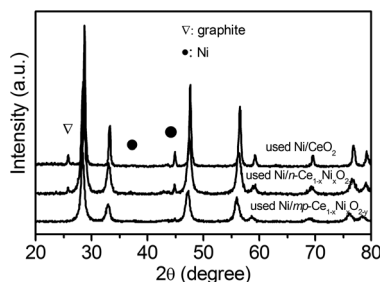**Fig. 8** The results of the stability test over the samples.

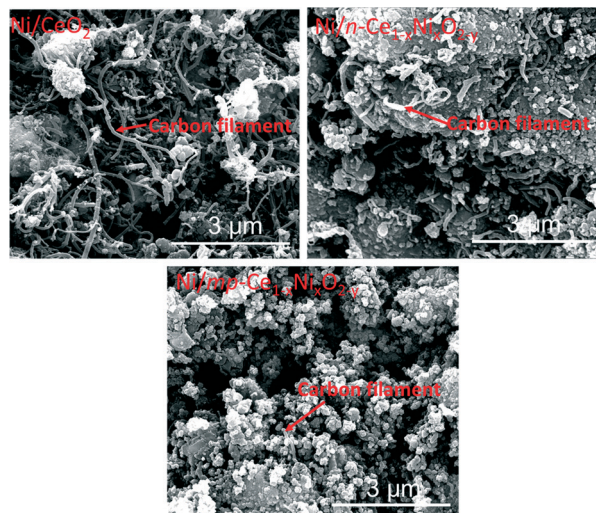**Fig. 9** XRD patterns of used Ni/CeO$_2$ (1200 min), Ni/n-Ce$_{1-x}$Ni$_x$O$_{2-y}$ (2400 min), and Ni/mp-Ce$_{1-x}$Ni$_x$O$_{2-y}$ (2400 min).

Fig. 10 SEM images of used Ni/CeO$_2$ (1200 min), Ni/n-Ce$_{1-x}$Ni$_x$O$_{2-y}$ (2400 min), and Ni/mp-Ce$_{1-x}$Ni$_x$O$_{2-y}$ (2400 min).
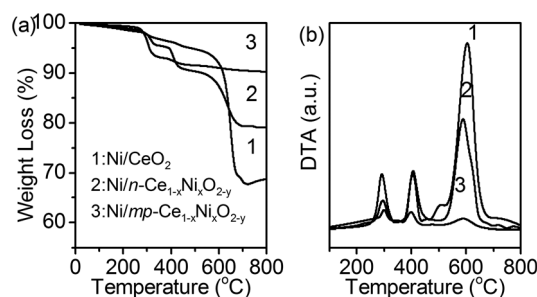

Fig. 11 (a) TG and (b) DTA profiles of used Ni/CeO$_2$ (1200 min), Ni/n-Ce$_{1-x}$Ni$_x$O$_{2-y}$ (2400 min), and Ni/mp-Ce$_{1-x}$Ni$_x$O$_{2-y}$ (2400 min).

Ni/CeO$_2$ > Ni/n-Ce$_{1-x}$Ni$_x$O$_{2-y}$ > Ni/mp-Ce$_{1-x}$Ni$_x$O$_{2-y}$, and their corresponding coking rates were Ni/CeO$_2$ > Ni/n-Ce$_{1-x}$Ni$_x$O$_{2-y}$ > Ni/mp-Ce$_{1-x}$Ni$_x$O$_{2-y}$, respectively. This showed that the scenario of coupling the mesostructure with the intermixed metal oxide played an important role in oppressing the carbon deposition. DTA curves of the catalysts indicated that an exothermal process, *viz.*, oxidation of the deposited carbon, occurred. Three exothermic peaks were detected in the DTA profiles of the spent samples, suggesting the existence of three kinds of carbon residuals with the various reactivities formed on the Ni active sites. It has been well documented that different types of carbon species can be formed on Ni-based catalytic materials due to CH$_4$ complete decomposition (CH$_4$ → C + 2H$_2$) and the Boudouard reaction (2CO → CO$_2$ + C).[67–69] And oxidizing the inactive carbons needed a much higher temperature relative to the reactive carbons. Hence, exothermic peaks at low temperatures between 170 and 300 °C represented the burning of the reactive carbon (C$_\alpha$), which was an active intermediate carbonaceous species for the production of syngas. Peaks ranging from 300 to 420 °C were ascribed to the less active amorphous carbons (C$_\beta$), which were formed from α-carbon by further dehydrogenation, polymerization, and rearrangement when lacking in

oxidant species or at lower oxidizing rates. The exothermic peaks at high temperatures above 600 °C were linked with the oxidation of inert carbons with various extents of graphitization (C$_\gamma$), which was hard to remove and can cause catalytic materials to finally deactivate. C$_\gamma$ was produced when C$_\beta$ dissolved in Ni crystals, then precipitated, nucleated, and grew into the filament-shaped graphitic carbons. Obviously, C$_\alpha$ was mainly detected on Ni/mp-Ce$_{1-x}$Ni$_x$O$_{2-y}$, while C$_\beta$ and C$_\gamma$ were predominant for Ni/CeO$_2$ and Ni/n-Ce$_{1-x}$Ni$_x$O$_{2-y}$. This implied that modification of the surface configuration or structure of Ni/mp-Ce$_{1-x}$Ni$_x$O$_{2-y}$ effectively prevented the nucleation and growth of carbon, leading to a good equilibrium between the carbon deposition and its removal. Overall, Ni/mp-Ce$_{1-x}$Ni$_x$O$_{2-y}$ had a good resistance to carbon deposition while the main reason for the fast deactivation over Ni/CeO$_2$ and Ni/n-Ce$_{1-x}$Ni$_x$O$_{2-y}$ could be explained as the carbon formation from CH$_4$ decomposition or the Boudouard reaction which could not be timely eliminated by the CO$_2$-derived oxygen species.

Structure–activity relationship

In this work, the one-step thermo-chemical conversion of notorious greenhouse gases into clean H$_2$ energy and versatile syngas was studied on different Ni–CeO$_2$ catalysts. Tuning the morphostructure of the nanocatalysts was found to be potentially advantageous to CRM. The exceptional behavior was reflected in the high initial activity, excellent anti-coking/sintering, and good long-term stability. The effective engineering with these attractive advantages was fulfilled by integrating the mesoporous framework with the intermixed metal oxide to directly construct a Ni NP-confined mesoporous Ce–Ni solid solution heterostructure using simple procedures. According to prior studies,[7–9] a carrier-mediated redox bifunctional mechanism for CRM using metal NPs anchored on reducible carrier materials is strongly suggested. As shown in Scheme 2: (1) CH$_4$ dissociates on metals to CH$_x$ + H*; (2) H* partially reduces the carrier in metal peripheries; (3) CO$_2$ decomposes on the carrier near metal NPs to CO + O*; (4) various O species on the carrier are transported onto metals to clean it from coke; and (5) O* re-oxidizes the carrier. By the steps above, a dynamic equilibrium is well built to keep a sustainable activity. In light of this mechanism, the good behavior of the Ni/mp-Ce$_{1-x}$Ni$_x$O$_{2-y}$
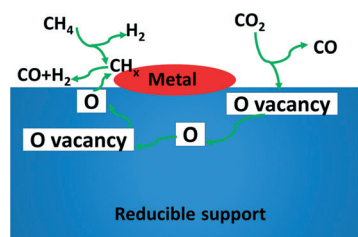
Scheme 2 Mechanic illustration of CRM over the metal/reducible supports.

nanocomposite can be collaboratively dominated by the following unique features.

First, the synergic effect between Ni and CeO_2, as shown by the TPR, altered the electronic structure of Ce and Ni and thus modified the adsorption/desorption behavior of the reactant species over them. Actually, the interplay between Ni and CeO_2 was an electronic interaction in that Ce is rich in d-electrons and Ni possesses unfilled d-orbitals which can accept d-electrons from Ce leading to an increment in the d-electron density of the Ni atom.[70–72] Dissociation of CH_4 preferentially occurs when the empty anti-bonding orbital of the C–H bond σ^* of the CH_4 molecules interacts with the high density of the occupied Ni 3d states near the Fermi levels.[73] Thus, the donating nature of the enhanced Ni 3d band states reinforced the interplay between the d states and σ^*, activating the adsorbate CH_4 molecules bonded to the Ni sites. Besides, as clearly unravelled by the structural/electronic data above, the surfaces of the mesostructured fluorite-type Ce–Ni solid solutions were defect-sufficient (such as oxygen vacancies and Ce^{3+} cations), and these defect sites were positively charged. In addition to enhancing the dispersion of the reduced Ni over mixed oxide surfaces, the oxophilic defect sites on Ni/mp-$Ce_{1-x}Ni_xO_{2-y}$ can also strongly attract negatively charged O atoms in CO_2 molecules, loosen, and cleave C–O bonds to dissociate CO_2 with concurrent formation of O species adsorbed on defective sites.[3,74] More importantly, because of the low reduction enthalpy or small oxygen activation/diffusion energy barrier, as shown by TPR, these O species on CeO_2 can be rapidly transferred or spilled over to contacted metal–support interface perimeters via the Mars–van Krevelen redox cycle mechanism so that CH_x fragments from CH_4 dissociation on active metal surfaces were timely oxidized by these oxygen species into H_2 and CO prior to their massive buildup and transition to graphitic carbons, thus effectively refreshing the Ni active sites. The substantial CO and syngas formation shown by activity even at very low temperatures indicated the efficient dissociative activation of reactants at the active centres. Such enhanced adsorption of both CO_2 on defects sites and CH_4 on Ni sites expedited the formation rate for oxidant species and CH_x fragments, respectively, and thus promoted the H_2 and syngas production activity. The low coking rate and the good O availability clearly suggested that the O transfer rate was rapid enough to match or emulate the CH_4 dissociation rate, and thus a dynamic balance between carbon formation and its removal was well established. In contrast, for Ni/CeO_2 and Ni/n-$Ce_{1-x}Ni_xO_{2-y}$, defect-deficient CeO_2 surfaces and the low density of occupied Ni 3d states lowered the affinity to oxidic CO_2 donor electrons and oxophilic CH_4 acceptor electrons, respectively.

Secondly, the size effect of the highly dispersed Ni NPs also contributed a lot to the behavior. It has been found that the coking rate and crystalline structures of carbon deposits are highly dependent on the Ni NP sizes.[75–78] Ni NPs below a certain critical size range will have a low growth rate and small yield for carbon filaments. This is because small sized

Ni crystallinities have a large carbon saturation concentration, which thus induces a small driving force for atomic carbons to dissolve in Ni clusters, then precipitate, nucleate, and finally grow into carbon filaments. Despite the close initial Ni NP size on the two mixed samples, it stayed stable on Ni/mp-$Ce_{1-x}Ni_xO_{2-y}$ but was very sintered on Ni/n-$Ce_{1-x}Ni_xO_{2-y}$ during the reaction. The increased NP size can have some consequences: (1) loss of available Ni sites limiting CH_4 activation; (2) a decrease of interface areas deterring the O transfer from CeO_2 across boundaries; and (3) augmentation of the driving force for the carbon filament growth. Thus, an acute imbalance of carbon formation rate and its removal rate occurred over the reaction time, yielding abundant filament cokes. Since carbon filaments are highly crystalline and thermally stable, they cannot be removed under CRM conditions once they are formed. As evidenced, carbon filaments can encapsulate active Ni phases, destroy catalyst structures, block catalyst beds, and eventually deactivate catalysts. And the diameter of the carbon filaments is determined by the size of the Ni NPs, and a typical diameter of carbon filaments (15–30 nm) is much larger than the size of the Ni NPs of Ni/mp-$Ce_{1-x}Ni_xO_{2-y}$. Thus, as shown by TGA, the lowest coking rate and the least crystalline and stable carbons were seen for Ni/mp-$Ce_{1-x}Ni_xO_{2-y}$ which had the smallest and most stable Ni NP size.

Thirdly, the mesoporous framework provided a particular confinement effect. Via elaborately modulating the synthesis technology within our current study, comparably nanosized Ni NPs were highly distributed on nonporous and mesoporous fluorite-type Ce–Ni solid solution. Yet, Ni NPs presented a distinct anti-clustering function under CRM conditions, with the highly dispersed Ni NPs being well maintained for Ni/mp-$Ce_{1-x}Ni_xO_{2-y}$ but significantly agglomerated for Ni/n-$Ce_{1-x}Ni_xO_{2-y}$. Given the similar preparation conditions, their distinct robustness against clustering was able to exclusively be ascribed to distinct porous systems. The large surface area mesostructure in Ni/mp-$Ce_{1-x}Ni_xO_{2-y}$ supplied enough inner concave channels to accommodate Ni NPs and thus led to an additional physical diffusion barrier for Ni NP migration. Therefore, the Ni growth and sintering was greatly impeded for the mesostructure. In addition, close contact of inner concave walls of mesopores with small sized Ni NPs can maximize the metal/support interfaces, which can further enhance the metal–support interaction and offer more boundary areas for oxygen/electrons to transport across, thereby greatly facilitating the occurrence of support-mediated redox bifunctional mechanisms. These advantages were not found in the case of the unconfined Ni NPs even though the Ni NPs before the reaction were ultra-small.

Conclusions

In summary, an enormous challenge to promote thermochemical catalysis of CRM is the identification of feasible catalysts. Industrial usages are built upon the low-cost and earth abundant materials that can operate under demanding

reaction conditions and meanwhile maintain a high and stable performance. Here, we demonstrate that all principal aspects of CRM heterogeneous nanocatalysts, including the small size of Ni NPs, interplay between Ni and CeO_2, and the good redox ability of support materials can be concurrently boosted by simply constructing the heterostructure of small sized Ni highly dispersed on mesoporous Ni-doped ceria. These multiple synergies resulted in exceptional catalytic behavior. The strategy here provides a desirable solution to the intrinsic issues of loaded metal catalysts for CRM, such as active phase sintering and coking. Interestingly, a notable behavior improvement can be fulfilled by introducing the randomly oriented mesoporosity and the mixed oxide. It can be expected that the subsequent amenability of the cubic fluorite-type ceria structure to doping/substitution, optimization of geometrical configuration, spatial orientation, periodic regularity, and physical diameter of the mesostructure, should open a tremendous engineering space, wherein even more efficient materials can be cogently explored. This will expedite industrial application of economical and sustainable energy source formation predicated upon thermo-chemically converting warming gases and broadly controlling catalytic properties for customized applications.

Acknowledgements

Notes and references

1 T. V. Choudhary and V. R. Choudhary, *Angew. Chem., Int. Ed.*, 2008, **47**, 1828–1847.

2 S. Perathoner and G. Centi, *ChemSusChem*, 2014, **7**, 1274–1282.

3 S. C. Yang, W. N. Su, J. Rick, S. D. Lin, J. Y. Liu, C. J. Pan, J. F. Lee and B. J. Hwang, *ChemSusChem*, 2013, **6**, 1326–1329.

4 R. Zhang, L. Guo, C. Chen, J. Chen, A. Chen, X. Zhao, X. Liu, Y. Xiu and Z. Hou, *Catal. Sci. Technol.*, 2015, **5**, 2959–2972.

5 P. Gao, L. Zhong, L. Zhang, H. Wang, N. Zhao, W. Wei and Y. Sun, *Catal. Sci. Technol.*, 2015, **5**, 4365–4377.

6 M. V. Landau, R. Vidruk and M. Herskowitz, *ChemSusChem*, 2014, **7**, 785–794.

7 M. S. Fan, A. Z. Abdullah and S. Bhatia, *ChemCatChem*, 2009, **1**, 192–208.

8 D. Liu, R. Lau, A. Borgna and Y. Yang, *Appl. Catal., A*, 2009, **358**, 110–118.

9 V. Sadykov, V. Rogov, E. Ermakova, D. Arendarsky, N. Mezentseva, G. Alikina, N. Sazonava, A. Bobin, S. Pavlova, Y. Schuurman and C. Mirodatos, *Thermochim. Acta*, 2013, **567**, 27–34.

10 Y. Y. Du, Q. Jin, J. T. Feng, N. Zhang, Y. F. He and D. Q. Li, *Catal. Sci. Technol.*, 2015, **5**, 3216–3225.

11 N. J. Divins, I. Angurell, C. Escudero, V. Pérez-Dieste and J. Llorca, *Science*, 2014, **364**, 620–623.

12 G. Zou, Y. Xu, S. Wang, M. Chen and W. Shangquan, *Catal. Sci. Technol.*, 2015, **5**, 1084–1092.

13 S. Sun, D. Mao, J. Yu, Z. Yang, G. Lu and Z. Ma, *Catal. Sci. Technol.*, 2015, **5**, 3166–3181.

14 Q. Fu, H. Saltsburg and M. Flytzani-Stephanopoulos, *Science*, 2003, **301**, 935–938.

15 J. A. Rodriguez, S. Ma, P. Liu, J. Hrbek, J. Evans and M. Pérez, *Science*, 2007, **318**, 1757–1760.

16 I. X. Green, W. Tang, M. Neurock and J. T. Yates Jr., *Science*, 2011, **333**, 736–739.

17 H. Liu, K. Tao, C. Xiong and S. Zhou, *Catal. Sci. Technol.*, 2015, **5**, 405–414.

18 C. M. A. Parlett, K. Wilson and A. F. Lee, *Chem. Soc. Rev.*, 2013, **42**, 3876–3893.

19 N. Wang, X. Yu, K. Shen, W. Chu and W. Qian, *Int. J. Hydrogen Energy*, 2013, **38**, 9718–9731.

20 N. Linares, A. M. Silvestre-Albero, E. Serrano, J. Silvestre-Albero and J. García-Martínez, *Chem. Soc. Rev.*, 2014, **43**, 7681–7717.

21 L. C. Chen, H. Cheng, C. W. Chiang and S. D. Lin, *ChemSusChem*, 2015, **8**, 1787–1793.

22 M. Almadi, A. Nambo, J. B. Jasinski, P. Ratnasamy and M. A. Carreon, *Catal. Sci. Technol.*, 2015, **5**, 380–388.

23 T. Hayakawa, H. Harihara, A. G. Andersen, A. P. E. York, K. Suzuki, H. Yasuda and D. K. Takehira, *Angew. Chem., Int. Ed. Engl.*, 1996, **35**, 192–195.

24 K. Takehira, T. Shishido, M. Kondo, R. Furukawa, E. Tanabe, K. Ito, S. Hamakawa and T. Hayakawa, *Stud. Surf. Sci. Catal.*, 2000, **130**, 3525–3530.

25 S. Surnev, A. Fortunelli and F. P. Netzer, *Chem. Rev.*, 2013, **113**, 4314–4372.

26 D. J. Stacchiola, S. D. Senanayake, P. Liu and J. A. Rodriguez, *Chem. Rev.*, 2013, **113**, 4373–4390.

27 J. Deng, M. Cai, W. Sun, X. Liao, W. Chu and X. S. Zhao, *ChemSusChem*, 2013, **7**, 2061–2065.

28 V. Papaefthimiou, M. Shishkin, D. K. Niakolas, M. Athanasiou, Y. T. Law, R. Arrigo, D. Teschner, M. Hävecker, A. Knop-Gericke, R. Schlögl, T. Ziegler, S. G. Neophytides and S. Zafeiratos, *Adv. Energy Mater.*, 2013, **3**, 762–769.

29 S. Mahammadunnisa, P. M. K. Reddy, N. Lingaiah and C. Subrahmanyam, *Catal. Sci. Technol.*, 2013, **3**, 730–736.

30 M. Gong, W. Zhou, M. C. Tsai, J. Zhou, M. Guan, M. C. Lin, B. Zhang, Y. Hu, D. Y. Wang, J. Yang, S. J. Pennycook, B. J. Hwang and H. Dai, *Nat. Commun.*, 2014, **4**, 1–6.

31 Q. Pan, J. Peng, S. Wang and S. Wang, *Catal. Sci. Technol.*, 2014, **4**, 502–509.

32 P. V. R. Rao, V. P. Kumar, G. S. Rao and K. V. R. Chary, *Catal. Sci. Technol.*, 2012, **2**, 1665–1673.

33 W. Zhou, F. Sun, K. Pan, G. Tian, B. Jiang, Z. Ren, C. Tian and H. Fu, *Adv. Funct. Mater.*, 2011, **21**, 1922–1930.

34 S. M. Morris, P. F. Fulvio and M. Jaroniec, *J. Am. Chem. Soc.*, 2008, **130**, 15210–15216.

35 D. Chandra, N. Abe, D. Takama, K. Saito, T. Yui and M. Yaqi, *ChemSusChem*, 2015, **8**, 795–799.

36 X. Du, D. Zhang, L. Shi, R. Gao and J. Zhang, *J. Phys. Chem. C*, 2012, **116**, 10009–10016.

37 T. Odedairo, J. Chen and Z. Zhu, *J. Phys. Chem. C*, 2013, **117**, 21288–21302.

38 J. Fan, D. Weng, X. Wu, X. Wu and R. Ran, *J. Catal.*, 2008, **258**, 177–186.

39 L. Pino, A. Vita, F. Cipitì, M. Laganà and V. Recupero, *Appl. Catal., B*, 2011, **104**, 64–73.

40 L. Meng, A. P. Jia, J. Q. Lu, L. F. Luo, W. X. Huang and M. F. Luo, *J. Phys. Chem. C*, 2011, **115**, 19789–19796.

41 Z. Liu, W. Xu, S. Yao, A. C. Johnson-Peck, F. Zhao, P. Michorczyk, A. Kubacka, E. A. Stach, M. Fernández-García, S. D. Senanayake and J. A. Rodriguez, *J. Catal.*, 2015, **321**, 90–99.

42 R. D. Shannon and C. T. Prewitt, *Acta Crystallogr., Sect. B: Struct. Crystallogr. Cryst. Chem.*, 1969, **25**, 925–946.

43 A. Gupta, U. Waghmare and M. Hegde, *Chem. Mater.*, 2010, **22**, 5184–5198.

44 J. A. Rodriguez, J. C. Hanson, J. Y. Kim, G. Liu, A. Iglesias-Juez and M. Fernández-García, *J. Phys. Chem. B*, 2003, **107**, 3535–3543.

45 Y. Al-Salik, I. Al-Shankiti and H. Idriss, *J. Electron Spectrosc. Relat. Phenom.*, 2014, **194**, 66–73.

46 R. Grau-Crespo, N. H. de Leeuw, S. Hamad and U. V. Waghmare, *Proc. R. Soc. A*, 2011, **467**, 1925–1938.

47 L. Barrio, A. Kubacka, G. Zhou, M. Estrella, A. Martínez-Arias, J. C. Hanson, M. Fernández-García and J. A. Rodriguez, *J. Phys. Chem. C*, 2010, **114**, 12689–12697.

48 X. Wang, J. A. Rodriguez, J. C. Hanson, D. Gamarra, A. Martínez-Arias and M. Fernández-García, *J. Phys. Chem. B*, 2005, **109**, 19595–19603.

49 J. A. Rodriguez, X. Wang, J. C. Hanson, G. Liu, A. Iglesias-Juez and M. Fernández-García, *J. Phys. Chem. B*, 2003, **119**, 5659–5669.

50 P. Zhi-Ying, J. Q. Liu, M. F. Luo and Y. L. Xie, *J. Phys. Chem. C*, 2007, **111**, 18695–18702.

51 M. Guo, J. Lu, Y. Wu, Y. Wang and M. Luo, *Langmuir*, 2011, **27**, 3872–3877.

52 Z. Wu, M. Li, J. Howe, H. M. Meyer and S. H. Overbury, *Langmuir*, 2010, **26**, 16595–16606.

53 L. Li, F. Chen, J. Q. Lu and M. F. Luo, *J. Phys. Chem. A*, 2011, **115**, 7972–7977.

54 R. Gao, D. Zhang, P. Maitarad, L. Shi, T. Rungrotmongkol, H. Li, J. Zhang and W. Cao, *J. Phys. Chem. C*, 2013, **117**, 10502–10511.

55 S. L. Zhong, L. F. Zhang, L. Wang, W. X. Huang, C. M. Fan and A. W. Xu, *J. Phys. Chem. C*, 2012, **116**, 13127–13132.

56 D. H. Prasad, S. Y. Park, H. I. Ji, H. R. Kim, J. W. Son, B. K. Kim, H. W. Lee and J. H. Lee, *J. Phys. Chem. C*, 2012, **116**, 3467–3476.

57 W. Y. Hernández, M. A. Centeno, F. Romero-Sarria and J. A. Odriozola, *J. Phys. Chem. C*, 2009, **113**, 5629–5635.

58 V. J. Ferreira, P. Tavares, J. L. Figueiredo and J. L. Faria, *Ind. Eng. Chem. Res.*, 2012, **51**, 10535–10541.

59 P. V. R. Rao, V. P. Kumar, G. S. Rao and K. V. R. Chary, *Catal. Sci. Technol.*, 2012, **2**, 1665–1673.

60 R. Pérez-Hernández, G. Mondragón-Galicia, A. A. Maravilla and J. Palacios, *Phys. Chem. Chem. Phys.*, 2013, **15**, 12702–12708.

61 L. Wang, H. Liu, Y. Liu, Y. Chen and S. J. Yang, *Rare Earths*, 2013, **31**, 559–564.

62 L. Jalowiecki-Duhamel, C. Pirez, M. Capron, F. Dumeignil and E. Payen, *Int. J. Hydrogen Energy*, 2010, **35**, 12741–12750.

63 G. Zhou, L. Barrio, S. Agnoli, S. D. Senanayake, J. Evans, A. Kubacka, M. L. Estrella, J. C. Hanson, A. Martnez-Arias, F. G. Marcos and J. Rodriguez, *Angew. Chem., Int. Ed.*, 2010, **49**, 1–6.

64 J. Z. Luo, Z. L. Yu, C. F. Ng and C. T. Au, *J. Catal.*, 2000, **194**, 198–210.

65 X. Chen, J. Jiang, S. Tian and K. Li, *Catal. Sci. Technol.*, 2015, **5**, 860–868.

66 D. Liu, X. Y. Quek, W. N. E. Cheo, R. Lau, A. Borgna and Y. Yang, *J. Catal.*, 2009, **266**, 380–390.

67 L. Mo, K. K. M. Leong and S. Kawi, *Catal. Sci. Technol.*, 2014, **4**, 2107–2114.

68 N. Wang, Z. X. Xu, J. Deng, K. Shen, X. Yu, W. Qian, W. Chu and F. Wei, *ChemCatChem*, 2014, **6**, 1470–1480.

69 Z. X. Xu, N. Wang, W. Chu, J. Deng and S. Luo, *Catal. Sci. Technol.*, 2015, **5**, 1588–1597.

70 M. A. Ebiad, D. R. Abd El-Hafiz, R. A. Elsalamony and L. S. Mohamed, *RSC Adv.*, 2012, **2**, 8145–8156.

71 Y. Yang, W. Li and H. Xu, *React. Kinet. Catal. Lett.*, 2002, **77**, 155–162.

72 F. Cova, D. G. Pintos, A. Juan and B. rigoyen, *J. Phys. Chem. C*, 2011, **115**, 7456–7465.

73 P. Kratzer, B. Hammer and J. K. Nørskov, *J. Chem. Phys.*, 1996, **105**, 5595–5604.

74 N. Sun, X. Wen, F. Wang, W. Peng, N. Zhao, F. Xiao, W. Wei, Y. Sun and J. Kang, *Appl. Surf. Sci.*, 2011, **257**, 9169–9176.

75 S. Q. Chen and Y. Liu, *Int. J. Hydrogen Energy*, 2009, **34**, 4735–4746.

76 Z. Li, X. Hu, L. Zhang, S. Liu and G. Lu, *Appl. Catal., A*, 2012, **417–418**, 281–289.

77 D. Baudouin, U. Rodemerck, F. Krumeich, A. de Mallmann, K. C. Szeto, H. Ménard, L. Veyre, J. P. Candy, P. B. Webb, C. Thieuleux and C. Copéret, *J. Catal.*, 2013, **297**, 27–34.

78 Q. Liang, L. Z. Gao, Q. Li, S. H. Tang, B. C. Liu and Z. L. Yu, *Carbon*, 2001, **39**, 897–903.